


The afterglow of GW170817 from every angle: Prospects for detecting the afterglows of binary neutron star mergers

Brian J. Morsony,¹  Ryan De Los Santos,² Rubin Hernandez,¹ Joshua Bustamante,¹

Brandon Yassuaie,¹ German Astorga,¹ and Juan Parra¹

¹*Department of Physics, California State University Stanislaus, One University Circle, Turlock, CA 95382, USA*

²*Department of Physics, The Ohio State University, 191 West Woodruff Ave., Columbus, OH 43210, USA*

Accepted XXX. Received YYY; in original form ZZZ

ABSTRACT

To date GW170817, produced by a binary neutron star (BNS) merger, is the only gravitational wave event with an electromagnetic (EM) counterpart. It was associated with a prompt short gamma-ray burst (GRB), an optical kilonova, and the afterglow of a structured, off-axis relativistic jet. We model the prospects for future mergers discovered in gravitational waves to produce detectable afterglows. Using a model fit to GW170817, we assume all BNS mergers produce jets with the same parameters, and model the afterglow luminosity for a full distribution of observer angles, ISM densities, and distances. We find that in the LIGO/Virgo O4 run, 30% - 50% of BNS mergers with a well-localized counterpart will have an afterglow detectable with current instrumentation in the X-ray, radio and optical. Without a previously detected counterpart, up to 18% will have an afterglow detectable by wide-area radio and optical surveys, compared to only about 5% of events expected to have bright (on-axis) gamma-ray emission. Therefore, most afterglows that are detected will be from off-axis jets. Further in the future, in the A+ era (O5), 50% - 60% of mergers will have afterglows detectable with next-generation X-ray and radio instruments. Future wide-area radio survey instruments, particularly DSA-2000, could detect 50% of afterglows, even without a kilonova counterpart. Finding and monitoring these afterglows will provide valuable insight into the structure and diversity of relativistic jets, the rate at which mergers produce jets, and constrain the angle of the mergers relative to our line of sight.

1 INTRODUCTION

GW170817 was the first BNS merger detected in gravitational waves (Abbott et al. 2017a), and was followed 1.7s later by a short gamma-ray burst, GRB170817A (Abbott et al. 2017c). Rapid optical followup associated this event with an optical transient in NGC4993 (Abbott et al. 2017c) at a redshift of $z = 0.0098$ (Hjorth et al. 2017). The optical transient is well fit by kilonova models (e.g. Cowperthwaite et al. 2017).

Although associated with intrinsically faint gamma-ray emission, initially there was no X-ray (Margutti et al. 2017) or radio emission (see Abbott et al. 2017c, and references therein) detected at the site of the kilonova that would indicate a relativistic afterglow. However, X-rays were detected by 9 days after the merger (Troja et al. 2017) and radio by 16 days (Mooley et al. 2017; Corsi et al. 2017; Hallinan et al. 2017). Afterglow luminosity increased by about a factor of 5 over the next 5 months, before beginning to decrease rapidly ($F_\nu \sim t^{-1.9}$, Makhathini et al. 2021), consistent with an off-axis relativistic jet. VLBI observations on days 75 and 230 showed superluminal motion of the radio source, with an apparent velocity of 4.1 ± 0.5 c (Mooley et al. 2018), confirming the presence of a relativistic jet aimed about 20° away from our line of sight.

Numerous modeling efforts (e.g. Lazzati et al. 2018; Mooley et al. 2018; Margutti et al. 2018; Lamb & Kobayashi 2018; Wu & MacFadyen 2018, 2019; Lin et al. 2019; Ioka & Nakamura 2019; Gill et al. 2019; Fraija et al. 2019; Troja et al. 2019; Hajela et al. 2019; Ziaeepour 2019; Beniamini et al. 2020; Cheng et al. 2021; Li & Dai 2021; Lamb et al. 2021; McDowell & MacFadyen 2023), both before and after the afterglow emission began to decline, are consistent with emission from a relativistic GRB jet seen 20° - 30° off-axis. The jet has a structured energy distribution, such that it has more energy closer to the jet axis. As the jet decelerated, light from material closer to the jet axis could be seen, leading to the brightness increasing over several months. Once the center was visible, the brightness began to decrease rapidly. This is the first definitive case where a) a GRB was seen off-axis and b) the jet was definitely structured, not just a flat energy distribution with a cutoff (top-hat jet).

Constraining the angle of the jet relative to Earth, combined with GW data, allows for better determinations of the Hubble constant than is possible with GW data alone. For example, the angle limits for GW170817 allowed the measurement of H_0 to be improved from $70.0^{+12.0}_{-8.0}$ km s⁻¹ Mpc⁻¹ (Abbott et al. 2017b) to $68.9^{+4.7}_{-4.6}$ km s⁻¹ Mpc⁻¹ (Hotokezaka et al. 2019). Just 16 BNS mergers with similar

quality jet angle determinations could constraint H_0 to less than 2% (Hotokezaka et al. 2019), compared to 50 - 100 needed without afterglow measurements.

Moving forward, the range of GW detectors will significantly increase. In O4, LIGO will be able to detect BNS out to 190 Mpc; in the A+ era (O5 run) this will increase to 325 Mpc (Abbott et al. 2020). This means there will be more BNS detected, but their EM counterparts will be significantly fainter for the same luminosity. We set out to determine what fraction of these mergers will have detectable afterglows.

This paper is organized as follows: In section 2 we outline our afterglow model and fitting procedure, and provide an updated fit to the afterglow observations of GW170817. In section 3 we model the fraction of GW events that will have a detectable afterglow accounting for observer angle and ISM density. We then explore how changes to GW horizon distance, EM instrument sensitivity, ISM density distribution, observation timing, and synchrotron electron index impact the fraction of detectable afterglows. In section 4 we summarize our conclusions.

2 METHODS

2.1 Afterglow Model

We model GRB afterglows using the semi-analytic Trans-Relativistic Afterglow Code (TRAC). This code was first used in Morsony et al. (2016) and is described in Appendix A. TRAC is available on GitHub¹ and the version used here is archived on Zenodo (Morsony 2023). The afterglow is modeled as an impulsive explosion expanding into an ISM with a constant particle density of n_{ISM} . This creates a shock that is tracked smoothly from its development through the ultrarelativistic phase and into the non-relativistic phase. Emission from the shock is assumed to be synchrotron radiation (see Appendix B) with electron powerlaw index p , electron energy fraction ϵ_e , and magnetic energy fraction ϵ_B , which are assumed to be the same at all positions and at all times for a given shock.

For the relativistic jet, we use a fixed jet profile taken from Lazzati et al. (2017). This energy distribution was produced by a relativistic hydrodynamical simulation of a jet propagating in the aftermath of a neutron star merger, and was previously used to fit the afterglow of GW170817 in Lazzati et al. (2018). This jet profile provides both the energy and initial mass of the ejecta as a function of angle from the jet axis. We assume a thickness of the ejecta of $\Delta = 3 \times 10^9$ cm (0.1 light-seconds) at all angles.

2.2 Fitting Procedure

To fit the afterglow of GW170817, we have 5 free parameters: n_{ISM} , observer angle θ_{obs} , p , ϵ_e , and ϵ_B . We fit to the observations of the afterglow of GW170817 from Makhathini et al. (2021), and the change in position of the afterglow from VLBI observations in Mooley et al. (2018). The change in position of our modeled afterglow is determined by creating a 2D afterglow image at the time and frequencies corresponding to the VLBI observations, then fitting a 2D Gaussian to the image, and taking the centroid position to be the location of the afterglow at that time. The difference between centroid locations is then the change in position.

We use Markov-Chain Monte Carlo (MCMC) to find the best fit of our 5 free parameters to the observations, using the emcee python package (Foreman-Mackey et al. 2013). However, running TRAC for a specific set of parameters is expensive. We therefore begin with an initial set of 90 afterglow models and interpolate between them for the MCMC fitting. The initial models cover a 4-dimensional space of $10^{-5} \leq n_{\text{ISM}} \leq 1$, $15 \leq \theta_{\text{obs}} \leq 35$, $2.05 \leq p \leq 2.35$, and $10^{-4} \leq \epsilon_B \leq 10^{-1}$. By assuming none of the observations are effected by synchrotron self-absorption, ϵ_e only changes the normalization of the modeled light curves. We therefore fix ϵ_e to 0.02 for all of our initial models. One model is run at each corner of the 4-dimensional space (16 models), one model at the center, and the remaining 73 models randomly distributed.

For each model, the brightness of the afterglow is calculated for 25 times, log spaced between 10^5 s and 10^9 s, and for 101 frequencies at each time, long spaced between 10^{-11} eV and 10^9 eV (2400 Hz to 2.4×10^{14} GHz), as well the change in location between VLBI observations. All models are carried out at redshift $z = 0.0098$ and luminosity distance $d_L = 40.4$ Mpc (Hjorth et al. 2017).

The initial models are first interpolated to the appropriate time and frequency for each observation. We can then interpolate between model parameters for each set of parameters needed for the MCMC fitting. Interpolation is carried out using Gaussian Process Regression (GPR), a machine learning technique (e.g. Rasmussen & Williams 2006). We use the sklearn python package (Pedregosa et al. 2011) and the Matérn kernel to create the GPR model. The interpolated models created with this technique are within a few percent of a full TRAC model run with the same parameters.

Finally, best fit parameters and error distributions are found using MCMC fitting over 5 free parameters, using our GPR-interpolated models for 4 parameters with the ranges listed above, and a normalization for ϵ_e , limited to $10^{-5} \leq \epsilon_e \leq 1$.

2.3 Best Fit for GW170817

Carrying out our fitting procedure on observations of GW170817 achieves a reduced chi-squared of 1.73. The best-fit parameters from fitting our structured jet model, and $1\text{-}\sigma$ errors, are shown in Table 1. These values are broadly consistent with previous fits (e.g. Lazzati et al. 2018; Mooley et al. 2018; Margutti et al. 2018; Wu & MacFadyen 2018, 2019; Hajela et al. 2019), with a low density ($\sim 10^{-3} \text{ cm}^{-3}$), small ϵ_B

¹ TRAC codebase: <https://github.com/morosny/TRAC>.

Parameter	Value	1- σ Error
n_{ISM}	$8.8 \times 10^{-4} \text{ cm}^{-3}$	$[-1.7, +2.0] \times 10^{-4} \text{ cm}^{-3}$
θ_{obs}	21.5°	$-0.5^\circ, +0.5^\circ$
p	2.127	$-0.005, +0.004$
ϵ_e	0.069	$-0.012, +0.012$
ϵ_B	8.1×10^{-4}	$[-1.5, +2.4] \times 10^{-4}$

Table 1. Best-fit parameters for the afterglow of GW170817, along with 1- σ error range

($\sim 10^{-3}$), and observer angle between 20 and 30 degrees. The inclusion of VLBI position data pushes our fit to a smaller angle. A corner plot of our fit parameters is shown in Fig. 1. There is significant degeneracy between ISM density and observer angle, with small angles and high densities both producing a bright, early peak, and between ϵ_e and ϵ_B , with high values of either producing a brighter afterglow.

Fig. 2 compares observations of GW170817 to our best-fit model. Between days 75 and 230, our model predicts an average apparent velocity of the radio afterglow of 3.4 c, within 1.5σ of the observed value of 4.1 ± 0.5 c from Mooley et al. (2018). Our model fits the data well, particularly for the rise and fall of the light curve. However, there are some discrepancies, as should be expected for a fixed jet profile. The peak of our fitted light curve is not quite as sharp or as bright as the observed peak, particularly in the radio. This is likely because our jet model flattens in the inner few degrees. An even more sharply peaked jet is needed to produce a sharper afterglow peak. Our model also under-predicts the brightness of the first X-ray detection. This could indicate our jet model has too much mass loading off-axis (the material directed towards Earth is travelling too slowly) producing a faint initial afterglow.

3 RESULTS

3.1 Detectability of GW afterglows over angle and density

With a best-fit model for GW170817 in hand, we can now examine how likely it is that future BNS mergers will have a detectable afterglow, assuming all mergers produce a GW170817-like jet. For our standard case, we assume the jet energy distribution and all parameters are the same as our best fit for GW170817, but we vary the distance, observer angle, and ISM density. We assume mergers are randomly distributed in space and observer angle, but account for the increased sensitivity of GW detectors to more face-on vs. edge-on mergers. For the ISM density distribution, we assume densities are equally likely in log space between 10^{-6} cm^{-3} and 10 cm^{-3} . This is consistent with the distribution of short GRB ISM densities found in Fong et al. (2015). The effects of modifying the density distribution are explored in section 3.4. For our standard assumptions, we model a GW horizon distance for face-on mergers of 200 Mpc, approximately what will be achieved for the LIGO O4 run (Abbott et al. 2020).

To determine if the afterglow of a merger is detectable, we set a threshold detection limit, then say an afterglow is detectable if it reaches a brightness at least double this limit at any point between 1 day and 1 year after the merger. This ensures an afterglow would be detected with reasonably spaced observations, but additional faint afterglows might be detectable with high-cadence observations.

We model the detectability of afterglows in X-ray, radio, and optical observations. For our standard assumptions on sensitivity, we assume targeted observations of a known source location, achievable with current instrumentation. This could be a location determined by, e.g., optical observations of a kilonova or a Swift-BAT gamma-ray counterpart. Our standard detection thresholds are $10^{-15} \text{ erg cm}^{-2} \text{ s}^{-1}$ for 0.3 – 10 keV X-ray observations (achievable with Chandra or XMM), 20 μJy at 6 GHz in radio (VLA), and 27th AB-magnitude in r-band optical observations (8-meter class telescope).

Under these assumptions, the afterglow of a GW170817-like event would have a 50% chance of being detectable in X-rays, a 32% chance in radio, and a 29% chance in optical for a GW horizon of 200 Mpc (see Table 2). Figs. 3 and 4 show the probability of an afterglow being detected vs. observer angle and ISM density. Our best fit to GW170817 has a hard electron spectrum ($p = 2.127$), making the X-ray afterglow relatively bright. Afterglows are brighter close to the jet axis and in denser environments, making the probability of being detectable higher at small angles and large densities. At the highest densities, in particular, all mergers would have a detectable afterglow, regardless of observer angle.

If Fig. 5, we show the detection probability vs. both angle and density in each band. There is a sharp transition between all events being detectable (within the GW horizon), and only a small fraction being detectable at close range. Note that most mergers with a detectable afterglow will not have bright gamma-ray emission directed at Earth. Taking 10° off-axis as the limit to have bright gamma-rays, only 5% of GW BNS mergers would be accompanied by a bright, classical short GRB, compared to up to 50% with a detectable afterglow. Of those events within 10° , the vast majority would have a detectable afterglow (95% in X-rays, 78% in radio, 76% in optical), with the exceptions being at very low densities.

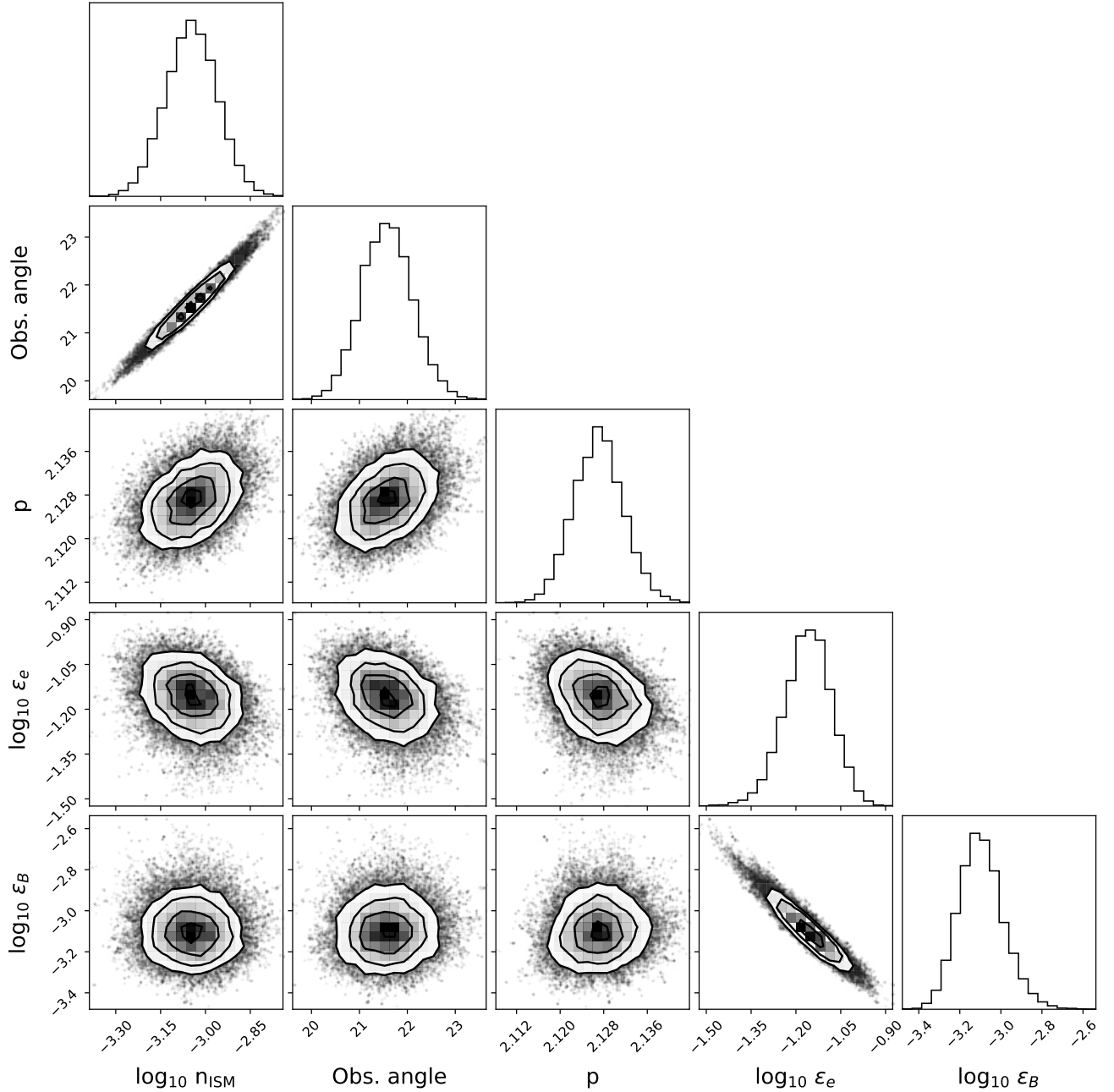


Figure 1. Corner plot of degeneracy in best-fit parameters for GW170817. There is degeneracy between ISM density and observer angle, and between ϵ_e and ϵ_B .

3.2 Impact of GW horizon distance

The distance at which BNS mergers can be detected will affect the fraction of mergers with detectable afterglows. As the sensitivity of GW detectors increases, the total number of detectable afterglows will increase. Fig. 6 shows the number of detectable afterglows per year as a function of the GW (on-axis) horizon distance. The total number of BNS mergers within the horizon are normalized to 1.5 mergers per year within 100 Mpc (Abbott et al. 2021). The dashed red line is the total number of BNS mergers. The number of detectable afterglows, with the standard assumption from section 3.1, increase roughly as horizon distance cubed out to a couple of hundred Mpc, the as distance squared (dotted purple line) beyond a Gpc.

Going from a horizon distance of 200 Mpc to 325 Mpc, appropriate for LIGO A+ era (O5 run), the number of BNS mergers per year

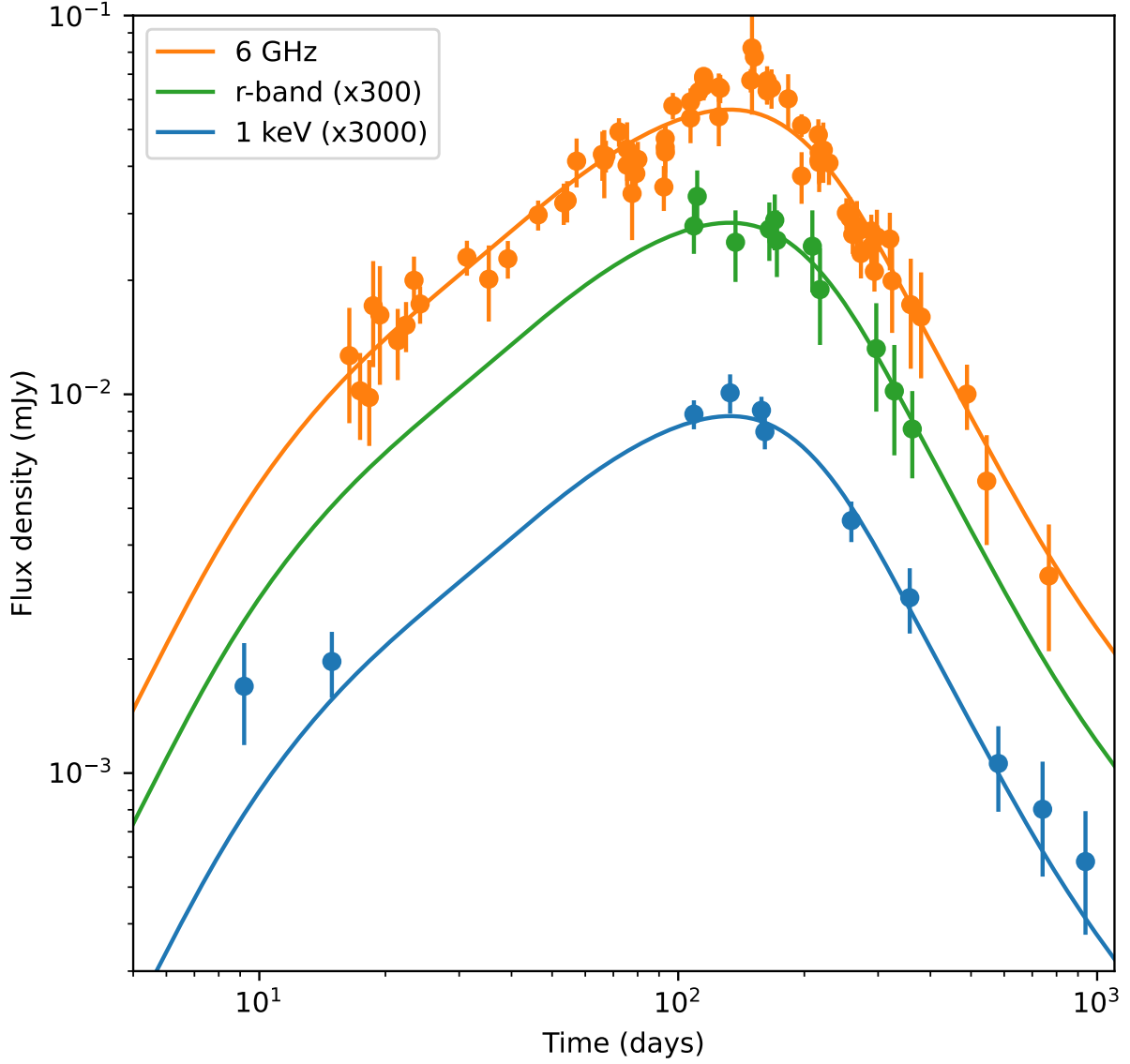


Figure 2. Comparison of observations of GW170817 (points with $1\text{-}\sigma$ error bars) and best-fit model (lines). Data is plotted for flux density in radio normalized to 6 GHz (orange), optical normalized to r-band (green), and X-ray at 1 keV (blue).

increases from 12 to 52, while the number of detectable X-ray afterglows goes from 6 to 22. The detectable fraction is about 8% less in all bands, dropping to 42% in X-ray, 24% in radio and 22% in optical (see Table 2).

We can also plot the detection probability as a function of GW strain, a quantity directly measurable from GW observations. Fig. 7 plots the detection probability vs. strain-distance: the distance a face-on BNS merger would be at to produce the detected strain. For example, at 43 Mpc, the approximate strain-distance of GW170817, the probability of having a detectable afterglow is 62%, 45%, and 43% in the X-ray, radio, and optical, respectively. At 200 Mpc, and at our best-fit observer angle and ISM density, GW170817 would not have had a detectable afterglow.

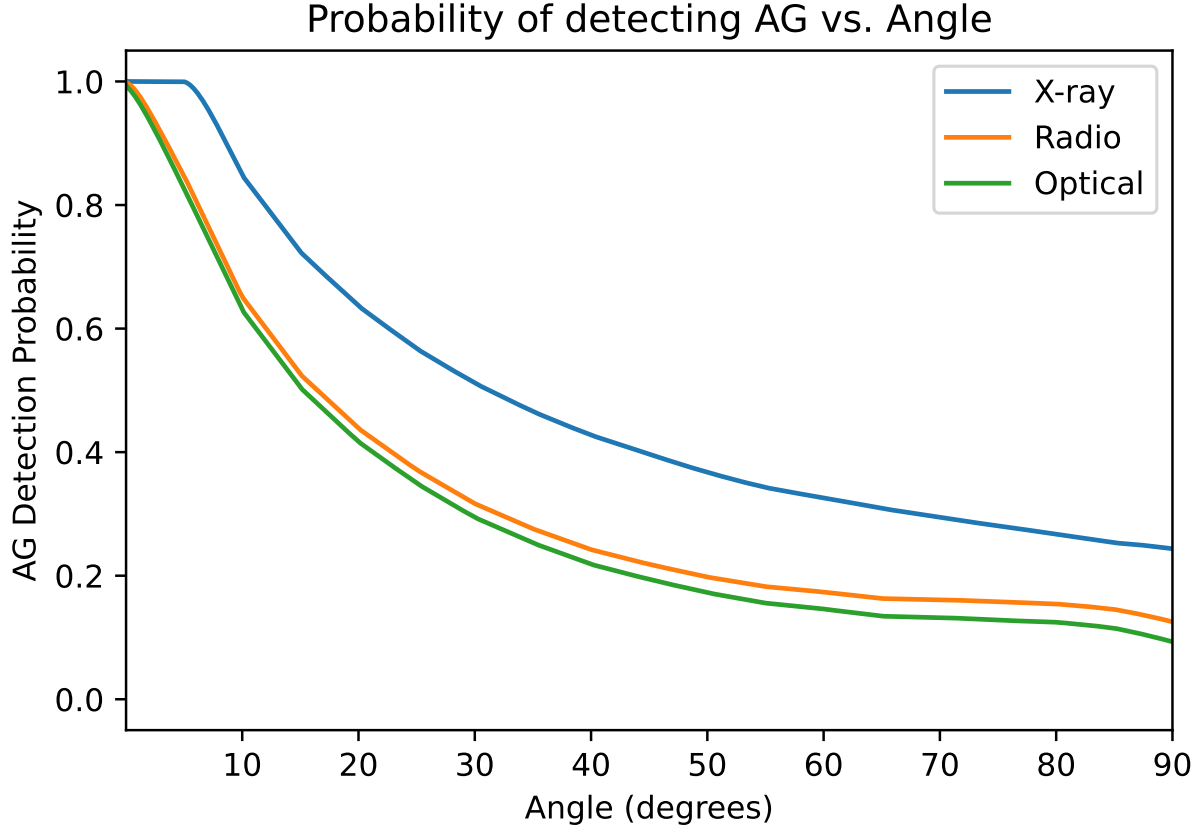


Figure 3. The probability of detecting the afterglow of a BNS merger vs. observer angle, assuming a GW horizon of 200 Mpc and our standard sensitivities (see section 3.1). Lines correspond to X-ray (blue), radio (orange), and optical (green) detection probabilities. On-axis afterglows tend to be brighter and hence more likely to be detected.

Model Name	Sensitivity			Horizon Distance (Mpc)	p-index	Density Distribution	Detection Probability		
	X-ray ($\text{erg cm}^{-2} \text{s}^{-1}$)	Radio (μJy)	Optical (AB mag)				X-ray	Radio	Optical
Standard	1.00e-15	20	27	200	2.1	Standard	50%	32%	29%
Standard A+	1.00e-15	20	27	325	2.1	Standard	42%	24%	22%
Survey	4.4E-14 ^a	250 ^b	24.5	200	2.1	Standard	11%	18%	13%
Survey A+	4.4E-14 ^a	250 ^b	24.5	325	2.1	Standard	7%	7%	8%
Next Gen	1.00e-16	2 ^b	30	200	2.1	Standard	65%	56%	50%
Next Gen A+	1.00e-16	2 ^b	30	325	2.1	Standard	59%	49%	44%
Low Dens	1.00e-15	20	27	200	2.1	$n < 1$	41%	21%	18%
Truncated Dens	1.00e-15	20	27	200	2.1	$10^{-4} < n < 1$	59%	30%	27%
$p = 2.5$	1.00e-15	20	27	200	2.5	Standard	27%	38%	21%
$p = 2.9$	1.00e-15	20	27	200	2.9	Standard	11%	39%	13%

^a between 0.5 and 2 keV

^b at 1 GHz

Table 2. Afterglow model parameters and detection probabilities. Column p-index is the electron index, with 2.1 corresponding to the best-fit value of 2.127. Standard density distribution is $10^{-6} < n_{\text{ISM}} < 10$, with densities in between equally distributed in log space. X-ray sensitivities are between 0.3 and 10 keV, and radio sensitivities are at 6 GHz, except where noted. All optical sensitivities are in r-band.

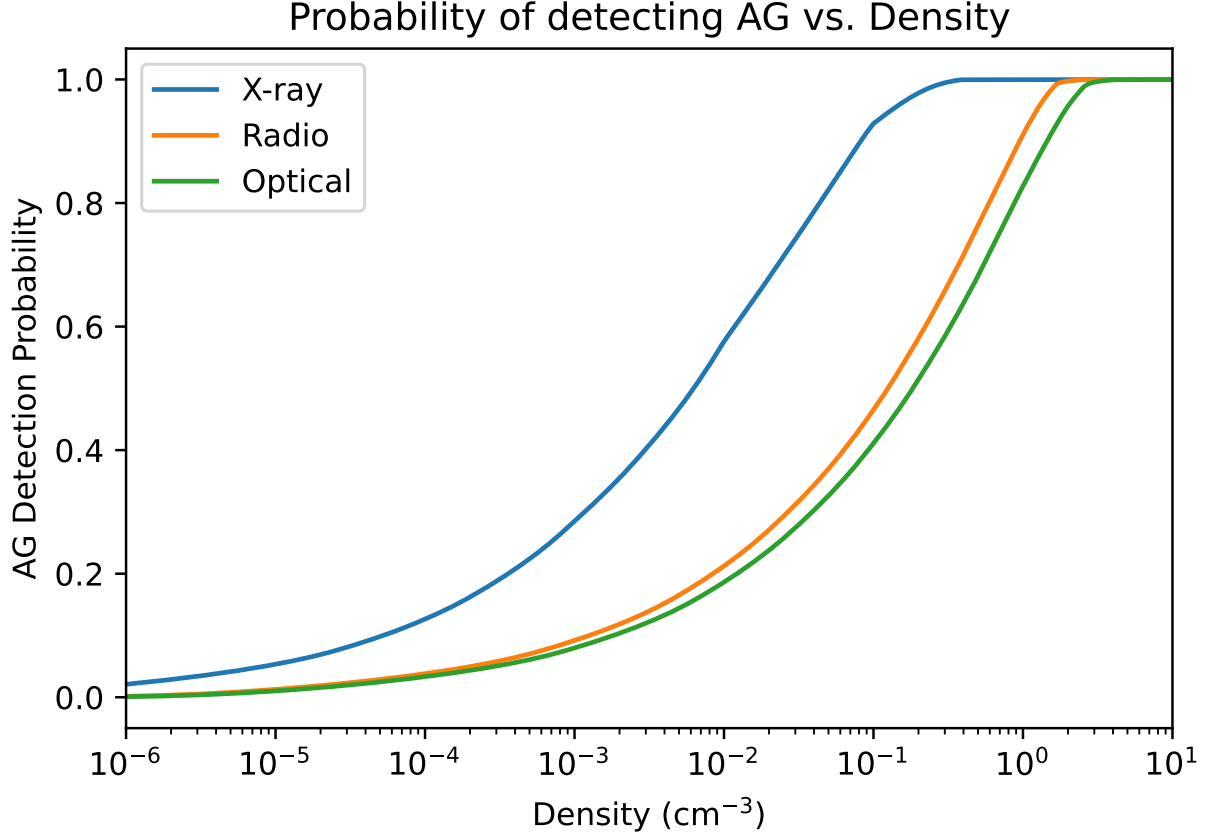


Figure 4. Same as Fig. 3, but for detection probability vs. ISM density. High densities produce brighter afterglow, which are more likely to be detected. For the highest densities, all mergers within the GW horizon would produce a detectable afterglow.

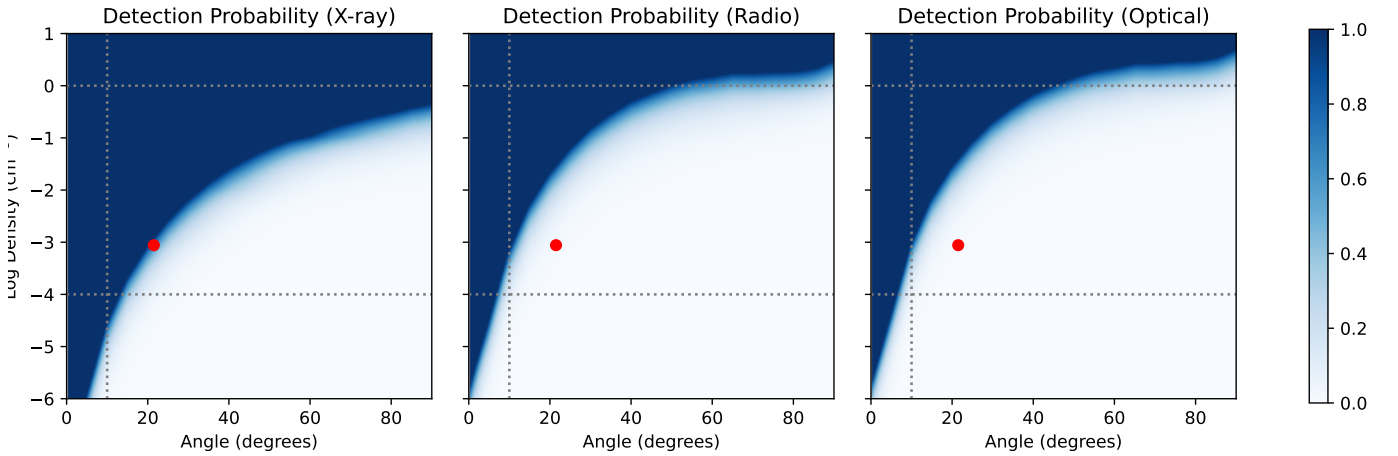


Figure 5. Each panel show the afterglow detection probability as a function of observer angle and ISM density for X-ray (left), radio (middle), and optical (right) observations, under our standard assumptions. Afterglows are most detectable at high densities and/or small angles, and fall off sharply at low densities and large angles. Horizontal dotted grey lines represent densities of 1 cm^{-3} and 10^{-4} cm^{-3} (see section 3.4). Vertical dotted grey line is at 10° , inside which a bright GRB would nominally be expected. The red dot in each panel is at the best-fit parameters for GW170817. At 200 Mpc, GW170817 would not have had a detectable afterglow.

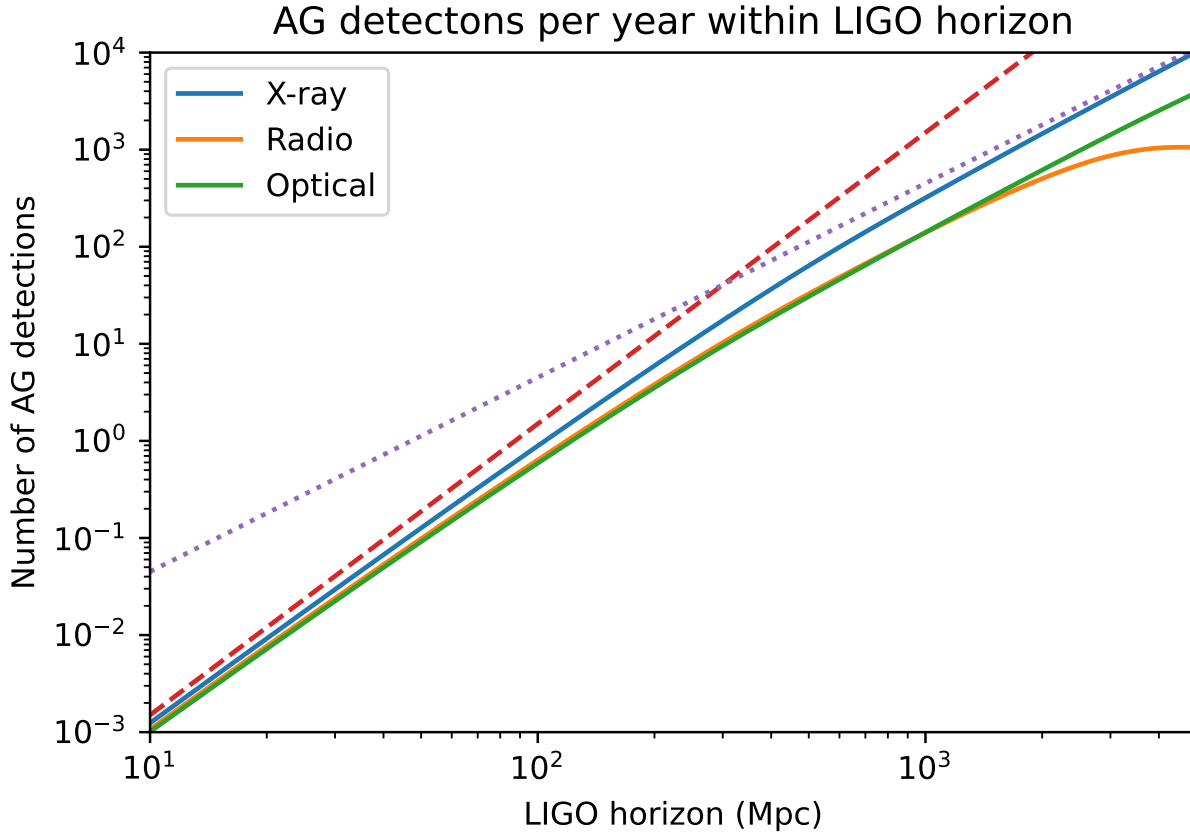


Figure 6. The total number of afterglows detectable per year, assuming our standard sensitivities, as a function of GW horizon distance. The dashed red line represents the number of BNS mergers detected per year, normalized to 1.5 mergers per year within 100 Mpc. The number of detectable afterglows increase as horizon distance cubed out to a couple hundred Mpc, then transitions and is proportional to roughly distance squared (dotted purple line) at Gpc distances.

3.3 Targeted vs. untargeted searches

We also explore the prospects for afterglow detection with different search sensitivities. We consider here a “survey” depth for untargeted searches and a “next gen” depth for near-future observing facilities.

For the survey sensitivity, we assume a GW detection but with no kilonova or other well-localized counterpart. Although not intended for this purpose, for the X-ray we set a threshold value of $4.4 \times 10^{-14} \text{ erg cm}^{-3} \text{ s}^{-1}$ from 0.5 to 2 keV for an eROSITA survey (Merloni et al. 2012). For radio, we assume a threshold of $250 \mu\text{Jy}$ at 1 GHz, achievable with ASKAP or Apertif. For optical, we assume a threshold of 24.5 AB-mag in r-band, for Rubin. The radio and optical surveys could be either purely serendipitous or targeted to a specific event. At the survey depths, a reasonable fraction of BNS mergers still have a detectable afterglow for a 200 Mpc GW horizon, particularly in the radio with 18% detectable (see Table 2). At larger distances, the detectable fraction falls rapidly to 7 – 8% at 325 Mpc. In Fig. 8, the detection rate in the radio cuts off rapidly beyond 200 Mpc. This is because synchrotron self-absorption is important at 1 GHz for afterglows at high densities.

For the “next gen” sensitivity, we assume well-targeted observations with future facilities. For X-rays, we use a threshold of $10^{-16} \text{ erg cm}^{-3} \text{ s}^{-1}$, possible with missions like Athena or AXIS (Piro et al. 2022; Mushotzky et al. 2019). For radio, we use a threshold of $2 \mu\text{Jy}$ at 1 GHz, possible with SKA Phase 1, ngVLA, or DSA-2000 (Braun et al. 2019; Selina et al. 2018; Hallinan et al. 2019), and for optical we assume a threshold of 30 AB-mag in r-band, possible with very deep HST or ground-based observations. Deeper observations detect significantly more afterglows, even at extended range (see Table 2).

Even with a 325 Mpc GW horizon for A+, more than 44% of afterglows are detectable in all bands, and 59% are detectable in X-rays, corresponding to about 30 afterglow detections per year. DSA-2000 will be able to survey large areas down to $2 \mu\text{Jy}$ (Hallinan et al. 2019), allowing an afterglow detection for about half of all A+ BNS mergers, even without a kilonova localization. In Fig. 9, the detection fraction remain high, $> 20\%$, even beyond 1 Gpc.

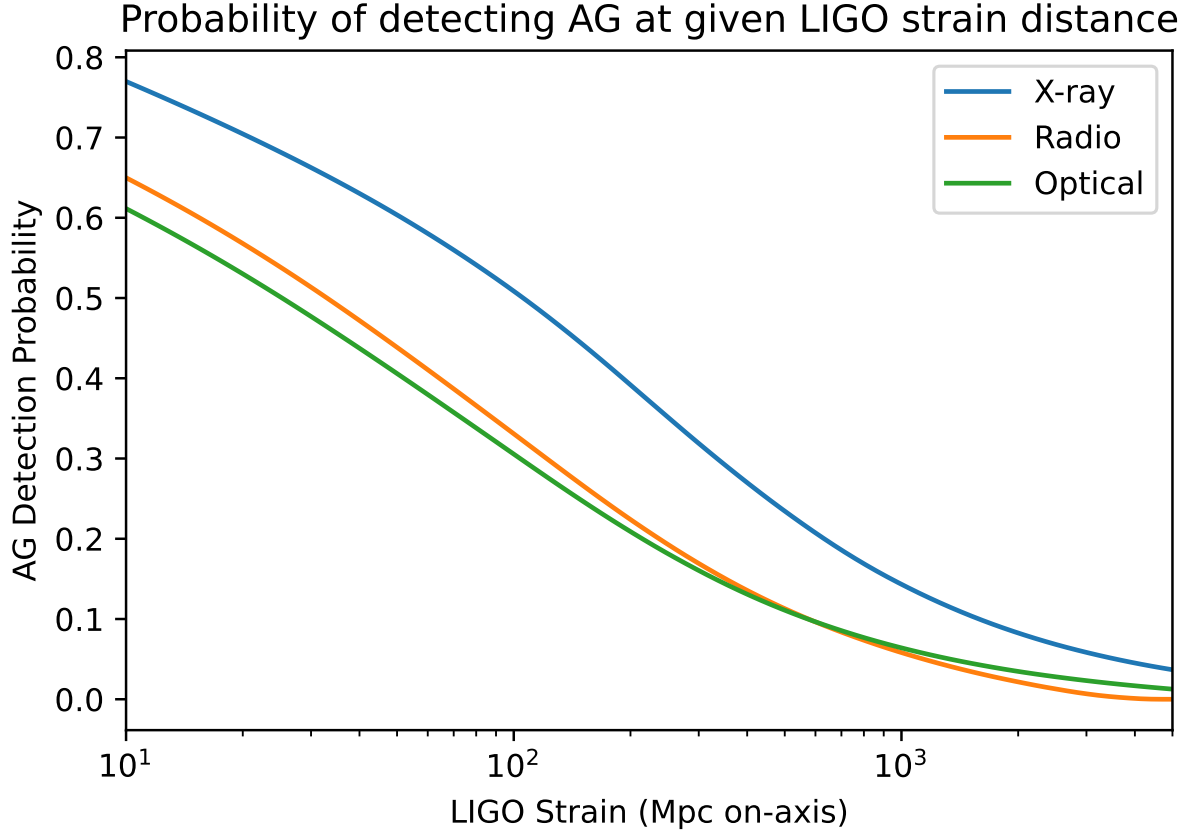


Figure 7. The probability that an afterglow will be detectable, assuming our standard sensitivities, for a BNS merger at a given GW strain, represented as the distance to a face-on BNS merger of the same strain in Mpc. At 43 Mpc, the approximate strain-distance of GW170817, the detection probability is 62%, 45%, and 43% in the X-ray, radio, and optical, respectively.

3.4 Impact of density distribution

The density of the ISM around BNS mergers is not well known. Although the distribution we choose is consistent with [Fong et al. \(2015\)](#), any deviations could have a strong affect on the number of detectable afterglows. For example, at high density almost all of the afterglows are detectable. If the density distribution is truncated at 1 cm^{-3} rather than 10 cm^{-3} , the detectability rate drops by about 10%, e.g. from 50% to 41% in X-ray (see Table 2). On the other hand, almost no afterglows are detectable at very low densities. Truncating the density distribution both below 10^{-4} cm^{-3} and above 1 cm^{-3} (dotted lines in Fig. 5), also a plausible distribution based on [Fong et al. \(2015\)](#), leads to almost no change in the detectability in the radio and optical and an increase in X-ray detectability, from 50% to 59%, under our standard assumptions.

3.5 Impact of timing of observations

Our default observing window extends from 1 day to 1 year after the BNS merger, with the requirement that the afterglow reach twice the threshold detection limit to be considered detectable. However, afterglows, particularly off-axis afterglows, are broadly peaked, so the timing of individual observations is not particularly critical. Fig. 10 shows the probability that an event will have a detectable afterglow (brighter than the threshold limit) on a given day for our standard model assumptions. This reaches up to a 44% chance of detecting an X-ray afterglow on day 106, compared to a 50% overall chance of being detectable. The radio and optical detection probabilities peak earlier in Fig. 10, because the afterglows detectable in those bands are at higher densities and/or smaller angles, meaning they peak earlier.

Due to the broad afterglow peak, the observing window can be shortened without significantly decreasing the number of detectable afterglows. For example, if the end of the observing window is shortened from 1 year to 3 months, the fraction of afterglows detectable only decreases by about 10%, e.g. from 50% to 45% for X-ray afterglows with our standard assumptions. In other words, by 3 months after the merger, 90% of all afterglows that will ever be detectable will have been bright enough to be detected. Ending observations at 6 months, the decrease in detectability is only about 5% compared to 1 year.

Delaying the start of the observing window also does not result in a significant decrease in the number of detectable afterglows. For example,

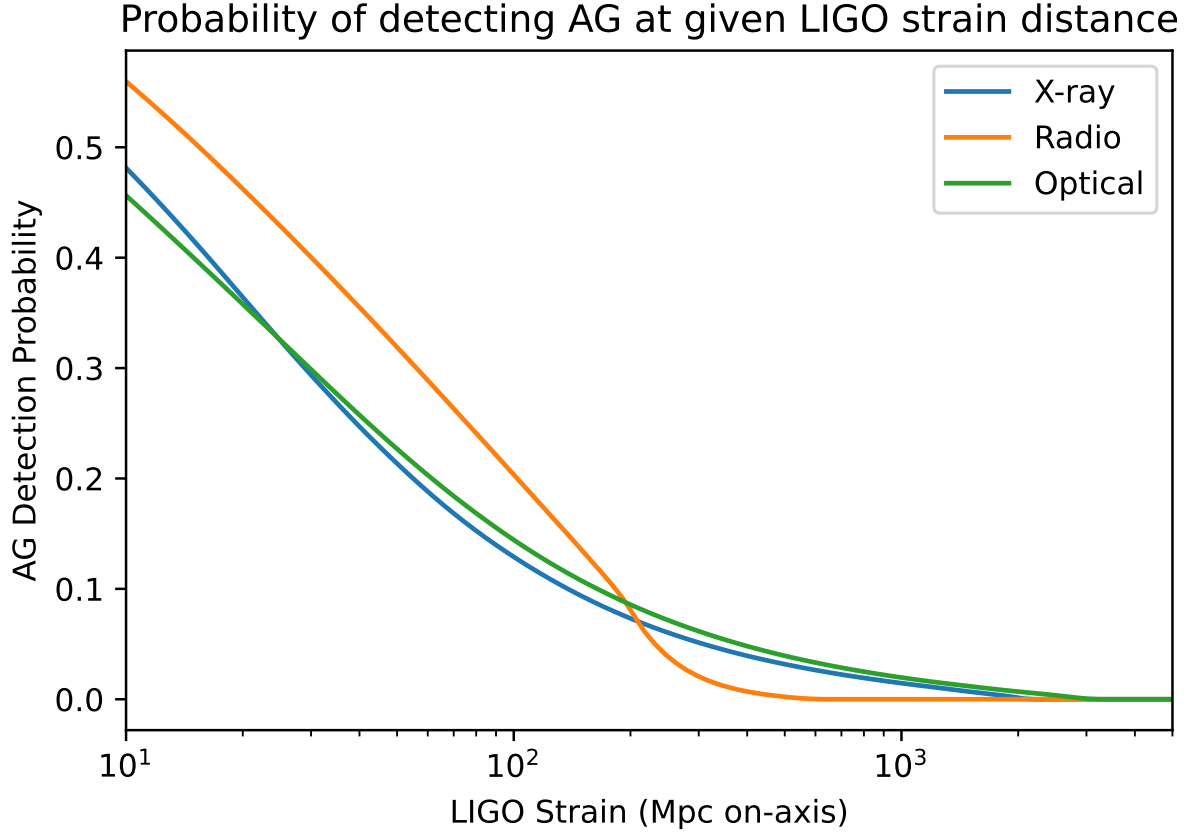


Figure 8. Same as Fig. 7, but for our survey depth sensitivities. There is a sharp cutoff in radio detectability beyond 200 Mpc due to synchrotron self-absorption.

delaying the start of observations from 1 day to 1 week only results in a $\sim 1\%$ decrease. However, early observations are critical for detecting the afterglow before it reaches its peak brightness, which is needed to constrain the observer angle and other afterglow parameters. In X-rays, with our standard model parameters, about 5% of detectable afterglows have already peaked at 1 day. By 1 week, 15% of X-ray afterglows have already peaked.

The situation is even worse as the fraction of afterglows that are detectable drops. For the “survey” sensitivity, 15% of the X-ray afterglows have passed their peak at 1 day, and 47% are past their peak by 1 week. Regardless of band, by the time at which an afterglow is most likely to be observable, (the peak of the curves in Figs. 10, 11, and 12) two-thirds of the detectable afterglows have already passed their peak.

3.6 Impact of p-index distribution

Our best fit model of GW170817 has a hard electron index of $p = 2.127$. We also consider softer electron indices of $p = 2.5$ and $p = 2.9$, both in the range of observed values for short GRBs (Fong et al. 2015). As p increases, the X-ray and optical flux decreases, making the afterglow more difficult to detect in these bands (see Table 2). The radio brightness, however, increases because there are more electrons at low energies. This increases the radio detectability from 32% to 38% and 39% at $p = 2.5$ and $p = 2.9$, respectively. For our standard sensitivities and GW horizon, this means there is almost a 40% chance an merger will have a detectable afterglow, either in the X-ray or radio, regardless of electron index.

Figs. 11 and 12 show the probability of having a detectable afterglow vs. time for these softer electron indices. In both cases, the probability of radio detection peaks at about 45 days, with earlier peaks for the X-ray and optical. For $p = 2.9$ (Fig. 12), the X-ray and optical detectability drop sharply after 10 days, emphasizing the need for early observations.

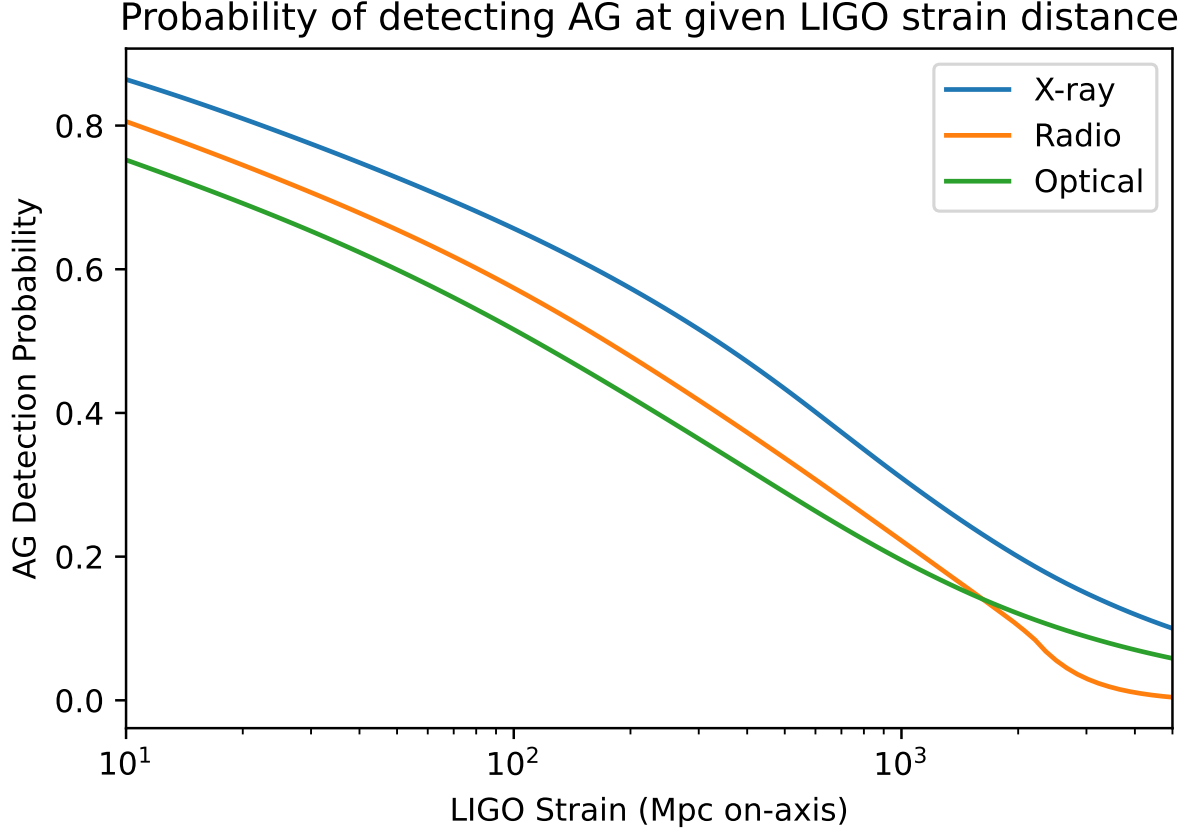


Figure 9. Same as Fig. 7, but for our “next gen” depth sensitivities. The radio sensitivity of $2 \mu\text{Jy}$ is achievable for DSA-2000 over large survey areas, enabling detection and localization of afterglows for a large fraction of BNS mergers, even without prior kilonova localizations.

4 CONCLUSIONS

The afterglow evolution of GW170817 is consistent with a structured, short GRB jet seen off-axis. Our updated best-fit parameters (Table 1), using a jet from a hydrodynamical simulation of a short GRB, find the jet observed about 21° off-axis, in a relatively low-density environment ($n_{\text{ISM}} \sim 10^{-3} \text{ cm}^{-3}$), consistent with previous models.

By assuming a) all BNS mergers produce a short GRB, b) all short GRB jets have the same structure, and c) all short GRB afterglows have the same shock parameters ($\epsilon_e, \epsilon_b, p$), we predict what fraction of BNS mergers will have afterglow bright enough to be detected. We find (see Table 2) that:

- In O4, 30% - 50% of BNS mergers will have an afterglow detectable with current instrumentation in the X-ray, radio, and/or optical, if the location of the merger is known from, e.g. a kilonova localization.
- Without preexisting EM localization, afterglows could still be detected in wide-area surveys. About 13% will have an optical afterglow detectable in deep optical surveys (i.e. Rubin) and 18% would be detectable in radio surveys (i.e. ASKAP and Apertif).
- In the LIGO A+ era (O5), the probability of an afterglow being detectable will increase, even as the distance increases, as next-generation instruments come online. In particular, DSA-2000 and SKA1 will be able to detect $\sim 50\%$ of radio afterglows, even without a prior EM localization. These facilities will be well matched by future X-ray facilities, such as Athena or AXIS.
- Changes to the assumed ISM density distribution can change the fraction of afterglows that will be detectable by about $\pm 10\%$.
- Afterglows with a softer electron index are significantly fainter in the X-ray and optical, but brighter in the radio. The combined X-ray and radio detection fraction is close to 40% during O4, regardless of electron index.
- Afterglows are most likely to be detectable between about 10 days and 3 months after the BNS merger, depending on what fraction are ultimately detectable. By 3 months, 90% of all afterglows that will ever be detectable will have become bright enough to be detected.
- Afterglows at smaller observer angles or in high-density regions are brighter and peak earlier. Therefore, when a lower detection fraction is expected, e.g. due to less sensitive instruments or farther distances, afterglows are most likely to be detected earlier.
- Early afterglow detections, before the afterglow reaches its peak brightness, are needed to constrain the jet structure and observer angle. For example, for X-rays in O4, about 5% of detectable afterglows will have peaked by 1 day, and 15% will have peaked by 1 week.

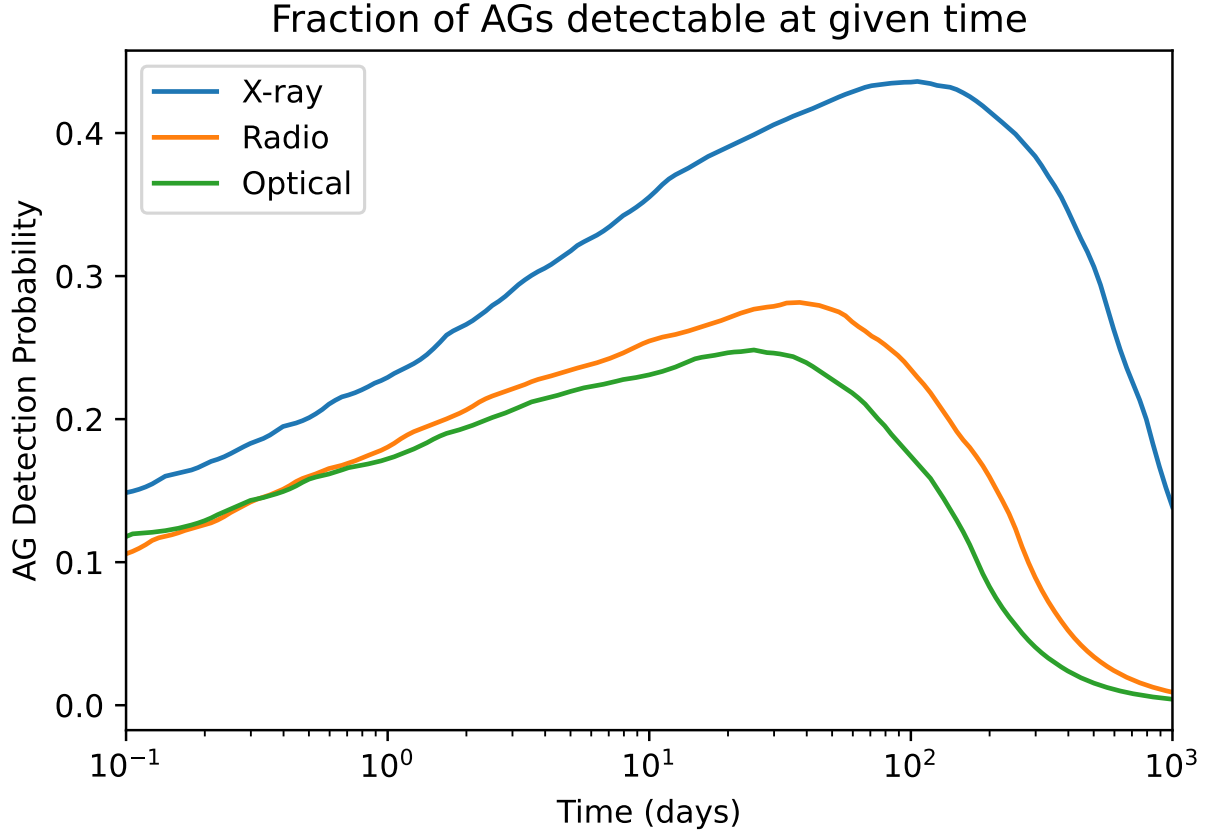


Figure 10. The probability of detecting an afterglow for an observation made at a given time after merger, for our standard sensitivities and a GW horizon of 200 Mpc. The curves peak at about 106 days, 38 days, and 25 days for X-ray, radio, and optical observations, respectively.

As the sensitivity of GW detectors, and the number of BNS mergers detected, increases, deep rapid multi-wavelength followup will be critical for detecting relativistic jets and determining the angle between any jet and our line of sight. Even in our worst case estimates, the number of afterglows that are detectable is far larger than the $\sim 5\%$ of BNS mergers that will be seen “on-axis” (within 10°) and are expected to be associated with bright, classical short GRBs. Most relativistic jets associated with mergers will be discovered through afterglow searches for off-axis jets. Modeling of the rates of afterglows detected, and modeling the light curves of individual events, will determine if all BNS mergers make jets, the distribution of energy and energy structure of those jets, and the angle at which individual jets are seen.

ACKNOWLEDGEMENTS

The authors thank Dr. Davide Lazzati and Isabel Rodriguez for their many useful discussions and inspiration that contributed to this project. We also thank Dr. Jared Work for his help in developing TRAC. This material is based upon work supported by the National Science Foundation under Grant No. 2218943. BJM and GA were supported in part by U.S. Department of Education PR/Award: P217A170182. This research activity is funded in part by the Stanislaus State STEM Success program through a U.S. Department of Education Title III grant #P031C160070. We gratefully acknowledge receiving support from the CSU-LSAMP Grant funded through the National Science Foundation (NSF) under grant #HRD-1826490 and the Chancellor’s Office of the California State University. This work was supported in part by Stanislaus State RSCA grant awards and the Student Engagement in Research, Scholarship, and Creative Activity (SERSCA) Program.

DATA AVAILABILITY

The observed afterglow brightnesses analyzed in this article were compiled in [Makhathini et al. \(2021\)](https://github.com/morsony/AG) and available at <https://github.com/kmooley/GW170817/>. VLBI position data can be found in [Mooley et al. \(2018\)](https://github.com/morsony/AG). Afterglow models were created using the version of TRAC archived in [Morsony \(2023\)](https://github.com/morsony/TRAC), available at <https://github.com/morsony/TRAC>.

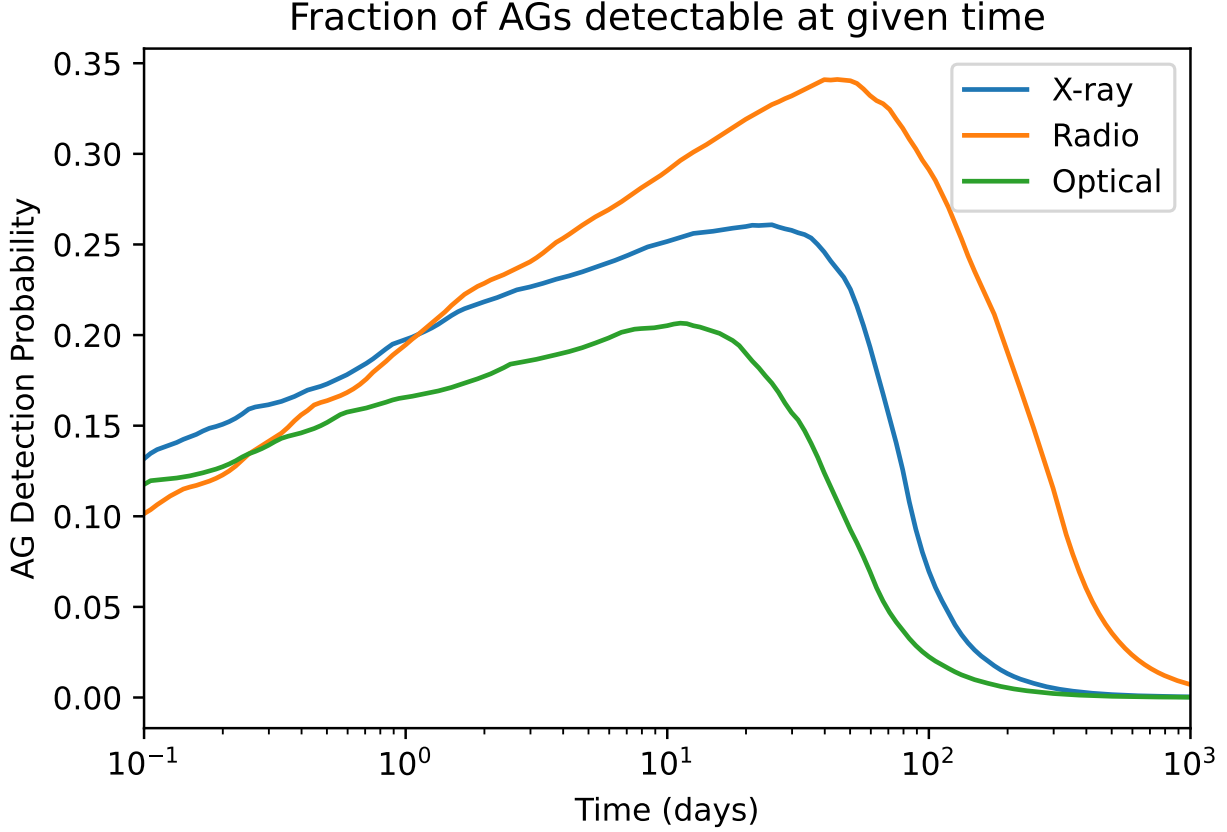


Figure 11. Same as Fig. 10 for electron index $p = 2.5$. The detection probability peaks at about 25 days in the X-ray, 45 days in the radio, and 11 days in the optical.

REFERENCES

- Abbott B. P., et al., 2017a, *Phys. Rev. Lett.*, **119**, 161101
 Abbott B. P., et al., 2017b, *Nature*, **551**, 85
 Abbott B. P., et al., 2017c, *ApJ*, **848**, L12
 Abbott B. P., et al., 2020, *Living Reviews in Relativity*, **23**, 3
 Abbott R., et al., 2021, *ApJ*, **913**, L7
 Beniamini P., Granot J., Gill R., 2020, *MNRAS*, **493**, 3521
 Blandford R. D., McKee C. F., 1976, *Physics of Fluids*, **19**, 1130
 Braun R., Bonaldi A., Bourke T., Keane E., Wagg J., 2019, *arXiv e-prints*, p. arXiv:1912.12699
 Cheng K.-F., Zhao X.-H., Zhang B.-B., Bai J.-M., 2021, *Research in Astronomy and Astrophysics*, **21**, 177
 Corsi A., Hallinan G., Mooley K., Frail D. A., Kasliwal M. M., Palliyaguru N. T., Growth Collaboration 2017, GRB Coordinates Network, **21815**, 1
 Cowperthwaite P. S., et al., 2017, *ApJ*, **848**, L17
 De Colle F., Granot J., López-Cámara D., Ramirez-Ruiz E., 2012, *ApJ*, **746**, 122
 Fong W., Berger E., Margutti R., Zauderer B. A., 2015, *ApJ*, **815**, 102
 Foreman-Mackey D., Hogg D. W., Lang D., Goodman J., 2013, *PASP*, **125**, 306
 Fraija N., Lopez-Cámara D., Pedreira A. C. C. d. E. S., Betancourt Kamenetskaia B., Veres P., Dichiaro S., 2019, *ApJ*, **884**, 71
 Gill R., Granot J., De Colle F., Urrutia G., 2019, *ApJ*, **883**, 15
 Granot J., Sari R., 2002, *ApJ*, **568**, 820
 Hajela A., et al., 2019, *ApJ*, **886**, L17
 Hallinan G., et al., 2017, *Science*, **358**, 1579
 Hallinan G., et al., 2019, in *Bulletin of the American Astronomical Society*. p. 255 (arXiv:1907.07648), doi:10.48550/arXiv.1907.07648
 Hjorth J., et al., 2017, *ApJ*, **848**, L31
 Hotokezaka K., Nakar E., Gottlieb O., Nissanke S., Masuda K., Hallinan G., Mooley K. P., Deller A. T., 2019, *Nature Astronomy*, **3**, 940
 Ioka K., Nakamura T., 2019, *MNRAS*, **487**, 4884
 Lamb G. P., Kobayashi S., 2018, *MNRAS*, **478**, 733
 Lamb G. P., et al., 2021, *Universe*, **7**, 329
 Lazzati D., López-Cámara D., Cantiello M., Morsony B. J., Perna R., Workman J. C., 2017, *ApJ*, **848**, L6
 Lazzati D., Perna R., Morsony B. J., Lopez-Cámara D., Cantiello M., Ciolfi R., Giacomazzo B., Workman J. C., 2018, *Phys. Rev. Lett.*, **120**, 241103

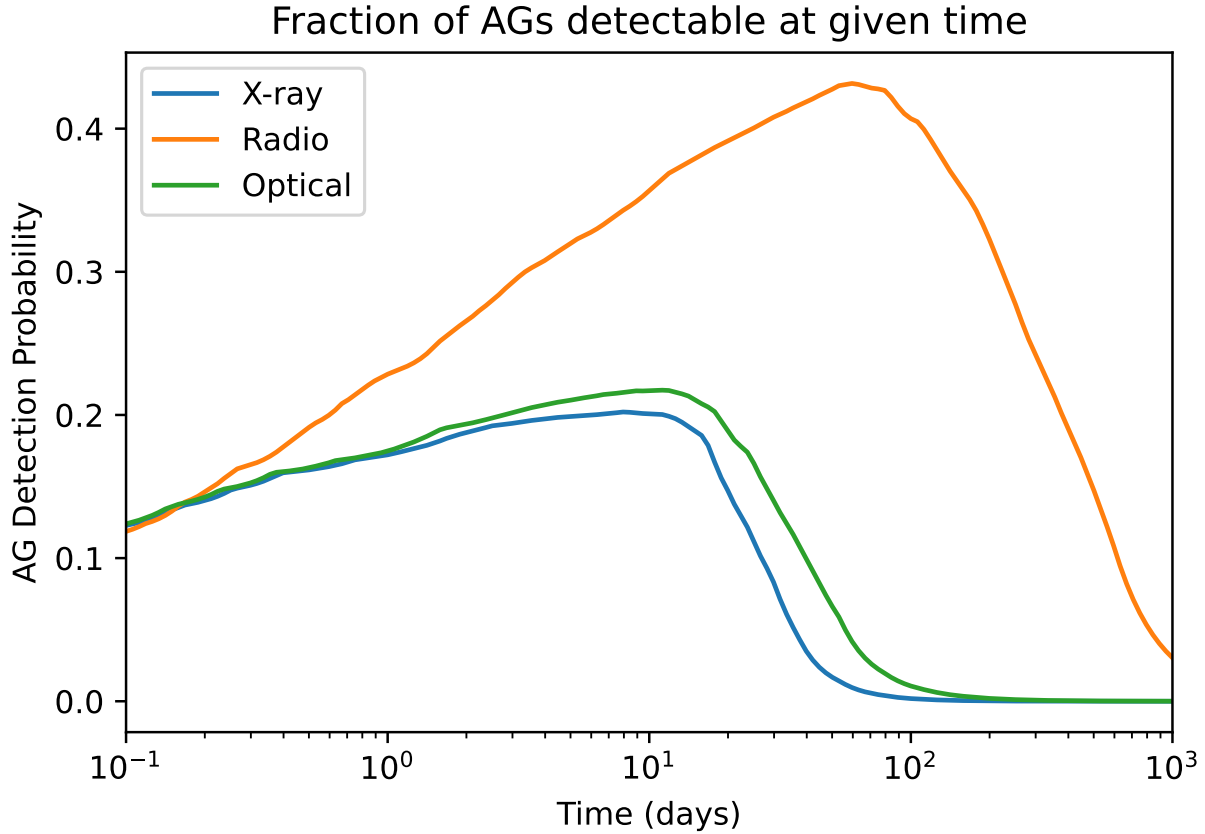


Figure 12. Same as Fig. 10 for electron index $p = 2.9$. The detection probability peaks at about 45 days in the radio. The X-ray and optical detectability both decline sharply after about 10 days.

- Li L., Dai Z.-G., 2021, *ApJ*, **918**, 52
- Lin H., Totani T., Kiuchi K., 2019, *MNRAS*, **485**, 2155
- Makhathini S., et al., 2021, *ApJ*, **922**, 154
- Margutti R., Fong W., Berger E., Chornock R., Cowperthwaite P., Alexander K. D., 2017, GRB Coordinates Network, **21648**, 1
- Margutti R., et al., 2018, *ApJ*, **856**, L18
- McDowell A., MacFadyen A., 2023, *ApJ*, **945**, 135
- Merloni A., et al., 2012, *arXiv e-prints*, p. [arXiv:1209.3114](https://arxiv.org/abs/1209.3114)
- Mooley K. P., Hallinan G., Corsi A., Jagwar Team Growth Team 2017, GRB Coordinates Network, **21814**, 1
- Mooley K. P., et al., 2018, *Nature*, **561**, 355
- Morsony B. J., 2023, TRAC, doi:10.5281/zenodo.7806800, <https://github.com/morsony/TRAC>
- Morsony B. J., Workman J. C., Ryan D. M., 2016, *ApJ*, **825**, L24
- Mushotzky R., et al., 2019, in Bulletin of the American Astronomical Society. p. 107 ([arXiv:1903.04083](https://arxiv.org/abs/1903.04083)), doi:10.48550/arXiv.1903.04083
- Pedregosa F., et al., 2011, *Journal of Machine Learning Research*, **12**, 2825
- Petruk O., 2000, *A&A*, **357**, 686
- Piro L., et al., 2022, *Experimental Astronomy*, **54**, 23
- Rasmussen C. E., Williams C. K. I., 2006, Gaussian Processes for Machine Learning
- Rybicki G. B., Lightman A. P., 1979, Radiative processes in astrophysics
- Sedov L. I., 1959, Similarity and Dimensional Methods in Mechanics
- Selina R. J., et al., 2018, in Marshall H. K., Spyromilio J., eds, Society of Photo-Optical Instrumentation Engineers (SPIE) Conference Series Vol. 10700, Ground-based and Airborne Telescopes VII. p. 107001O ([arXiv:1806.08405](https://arxiv.org/abs/1806.08405)), doi:10.1117/12.2312089
- Taylor G., 1950, *Proceedings of the Royal Society of London Series A*, **201**, 159
- Troja E., Piro L., Sakamoto T., Cenko S. B., Lien A., 2017, GRB Coordinates Network, **21765**, 1
- Troja E., et al., 2019, *MNRAS*, **489**, 1919
- Wu Y., MacFadyen A., 2018, *ApJ*, **869**, 55
- Wu Y., MacFadyen A., 2019, *ApJ*, **880**, L23
- Ziaepour H., 2019, *MNRAS*, **490**, 2822
- van Eerten H., 2014, *MNRAS*, **442**, 3495

APPENDIX A: AFTERGLOW CODE

The afterglow luminosity is calculated using a version of the TRAC afterglow code, first used in [Morsony et al. \(2016\)](#). Our code first uses a semi-analytic model to find the hydrodynamic properties of a relativistic blastwave (pressure, density, velocity), and then calculates the integrated synchrotron radiation.

To model the blastwave, we assume that at any angle relative to the jet axis there is a fixed isotropic equivalent energy, E , and a fixed initial amount of mass, m_0 . We assume there is no mixing between angles or spreading of the jet. This allows us to model the evolution at each angle as a uniform, spherical, impulsive explosion, expanding into a uniform medium. The location and velocity of the resulting shock can be found analytically in the ultra-relativistic limit by the Blandford-McKee solution ([Blandford & McKee 1976](#)) and in the non-relativistic limit by the Sedov-Taylor solution ([Sedov 1959; Taylor 1950](#)). We assume a relativistic temperature for the shocked material (adiabatic index of $\gamma_{ad} = 4/3$) at all times.

Originally, TRAC followed [De Colle et al. \(2012\)](#), to find a semi-analytic approximation to interpolate between the ultra- and non-relativistic limits, allowing us to follow the decelerating afterglow shock through the semi-relativistic regime. This has now been revised to a new interpolation based on comparison with 1D relativistic hydrodynamic simulations with a constant external density (see sec. A3).

We have also modified this interpolation to be valid in three phases: 1) the piston phase, where the mass of material from the explosion is much more than the mass that has been swept up, and the velocity (Lorentz factor) of the forward shock is comparable to that of the ejecta, 2) the wind-driven phase, where material from the explosion is still being swept up by a reverse shock, adding energy to the forward shock, and the velocity (Lorentz factor) of the forward shock is much less than that of the ejecta, and 3) the blastwave phase, where all the energy is in the forward shock, and the explosion can be treated as an impulsive energy injection. Depending on the thickness of the ejecta (or the duration of energy injection), the shock can transition directly from the piston to blastwave regimes, for narrow ejecta, or go from the piston to wind-driven to blastwave regimes, for thick ejecta.

A1 Piston Phase

In the piston phase, the ejecta acts as a solid piston, pushing mass in front. We can treat the swept-up mass as negligible, so that no deceleration is taking place. The contact discontinuity will move at β_0 , the initial speed of the ejecta. The density ratio in the comoving frame is:

$$\frac{\rho_f}{\rho_0} = \frac{\gamma_{ad}\Gamma_f + 1}{\gamma_{ad} - 1} \quad (\text{A1})$$

where $\gamma_{ad} = 4/3$ is the adiabatic index of the shocked gas, Γ_f is the Lorentz factor of the shocked gas, ρ_0 is the density of the unshocked ISM gas, and ρ_f is the density of the shocked gas at the shock. Behind the shock, we approximate the density and velocity of the gas as constant. In the lab frame, the density of the shocked gas will be

$$\rho'_f = \rho_0 \frac{\rho_f}{\rho_0} \Gamma_f \quad (\text{A2})$$

Using this density ratio, we can now find the approximate position, velocity and Lorentz factor of the shock in terms of Γ_f by mass conservation. For a constant external density, the mass swept up by the shock is

$$M_s = \frac{4\pi}{3} \rho_0 R_s^3 \quad (\text{A3})$$

and the volume between the shock and the contact discontinuity is

$$V_s = \frac{4\pi}{3} (R_s^3 - R_c^3) \quad (\text{A4})$$

where R_s is the radius of the shock at a given time and R_c is the radius of the contact discontinuity. Taking the density between R_s and R_c to be constant, we have

$$M_s = \rho'_f V_s = \rho_0 \frac{\rho_f}{\rho_0} \Gamma_f V_s \quad (\text{A5})$$

Rearranging the two equation for M_s , we obtain

$$R_s^3 = \frac{\rho_f}{\rho_0} \Gamma_f (R_s^3 - R_c^3) \quad (\text{A6})$$

or

$$\left(\frac{\rho_f}{\rho_0} \Gamma_0 - 1 \right) R_s^3 = \left(\frac{\rho_f}{\rho_0} \Gamma_0 \right) R_c^3 \quad (\text{A7})$$

Because we assume the velocities of the shock and ejecta are constant, we can substitute $R_s = \beta_s ct$ and $R_c = \beta_0 ct$, where β_s is the velocity of the shock and β_0 is the velocity of the ejecta. Solving for β_s^2 , we find

$$\beta_s^2 = \left(\frac{\Gamma_f}{\Gamma_f - \frac{\gamma_{ad}-1}{\gamma_{ad}\Gamma_f+1}} \right)^{2/3} \beta_0^2 \quad (\text{A8})$$

For an arbitrarily strong relativistic shock, the Lorentz factor of the shock in terms of Γ_f is given by (Blandford & McKee 1976):

$$\Gamma_s^2 = \frac{(\Gamma_f + 1) [\gamma_{ad}(\Gamma_f - 1) + 1]^2}{\gamma_{ad}(2 - \gamma_{ad})(\Gamma_f - 1) + 2} \quad (\text{A9})$$

which can be changed to an equation for β_s^2 as:

$$\beta_s^2 = 1 - \frac{\gamma_{ad}(2 - \gamma_{ad})(\Gamma_f - 1) + 2}{(\Gamma_f + 1) [\gamma_{ad}(\Gamma_f - 1) + 1]^2} \quad (\text{A10})$$

The we now have two equations for β_s^2 in terms of Γ_f , with the only free parameters being the adiabatic index, γ_{ad} , and the speed of the ejecta, β_0 . We can set eqn. A8 and eqn. A10 equal to each other and solve numerically to find $\Gamma_{s,p}$, the Lorentz factor of the shock in the piston phase.

In the ultra-relativistic limit, the Lorentz factor of the shock is:

$$\Gamma_{s,p} = \sqrt{\frac{4}{3}} \Gamma_0 \quad (\text{A11})$$

In the non-relativistic limit, the speed of the shock goes to:

$$\beta_{s,p} = \left(\frac{7}{6} \right)^{1/3} \beta_0 \quad (\text{A12})$$

A2 Wind Phase

For the wind phase, we model the shock as a blastwave with a continuous energy supply. Following Blandford & McKee (1976), van Eerten (2014) find that, for energy injected at a rate $L = L_0 t_e^q$, where t_e is the time of emission, the Lorentz factor of the shock in the ultrarelativistic limit is

$$\Gamma_s^2 = \left[\frac{L_0 \chi_{RS}^{1+q} c^{k-5}}{2^q (m+1)^q 16\pi \rho_0 R^k f_{RS}} \right]^{\frac{1}{2+q}} t^{\frac{q+k-2}{q+2}} \quad (\text{A13})$$

where χ_{RS} is the value of the similarity variable χ at the reverse shock, and f_{RS} is the pressure ratio $f(\chi_{RS}) = p_{RS}/p_f$. For continuous energy injection and an constant-density external medium, $q = 0$, $k = 0$, $m = 1$, $\chi_{RS} = 2.7$ and $f_{RS} = 0.449$. For a total (isotropic equivalent) energy injection E_0 and a physical thickness of the ejecta Δ , the value of L_0 will be

$$L_0 = \frac{E_0 c \beta_0}{\Delta} \quad (\text{A14})$$

Using L_0 and the approximation $t = R/c$, the ultrarelativistic equation for Γ_s is

$$\Gamma_s^2 = \left[\frac{\chi_{RS} E_0 \beta_0}{f_{RS} 16\pi \rho_0 \Delta} \right]^{\frac{1}{2}} R^{-1} c^{-1} \quad (\text{A15})$$

This equation is only valid in the ultrarelativistic limit, and has been derived with the assumptions that $\beta_s \rightarrow 1$ and $\Gamma_s^2 = 2\Gamma_f^2$. We can obtain a better equation for a mildly relativistic shock by rewriting eqn. A15 as an equation for $\Gamma_f^2 \beta_f^2$:

$$\Gamma_f^2 \beta_f^2 = \frac{1}{2} \left[\frac{\chi_{RS} E_0 \beta_0}{f_{RS} 16\pi \rho_0 \Delta} \right]^{\frac{1}{2}} R^{-1} c^{-1} \quad (\text{A16})$$

We can then use $\Gamma_f = \sqrt{\Gamma_f^2 \beta_f^2 + 1}$ to solve for $\Gamma_{s,w}$ using eqn. A9. This result provides a better fit to numerical simulations for mildly relativistic shocks and a guarantees a Lorentz factor > 1 for any value of R .

A3 Blastwave Phase

In the blastwave phase, the explosion can be treated as an impulsive injection of energy. The (isotropic equivalent) kinetic energy injected is defined as

$$E_0 = (\Gamma_0 - 1)m_0 c^2 \quad (\text{A17})$$

where Γ_0 is the initial Lorentz factor of the ejecta and m_0 is the initial mass of the ejecta. For a spherical shock expanding into a medium with density

$$\rho = \rho_0 R^{-k} \quad (\text{A18})$$

and the mass swept up by the shock at any given radius is

$$m_k = \frac{4\pi}{(3-k)} \rho_0 R^{3-k} \quad (\text{A19})$$

For ultrarelativistic ejecta, the mass of the ejecta is $m_0 = 0$, so the total mass contained in the shock is $m = m_k$. In the ultrarelativistic limit, following [Blandford & McKee \(1976\)](#), the energy contained in the shock is:

$$E_{rel} = \frac{8\pi}{17-4k} \rho_0 R^{3-k} c^2 \Gamma_s^2 \beta_s^2 \quad (\text{A20})$$

which we can rewrite as

$$E_{rel} = \frac{8\pi}{17-4k} \frac{(3-k)}{4\pi} m_k c^2 \Gamma_s^2 \beta_s^2 \quad (\text{A21})$$

Similarly, in non-relativistic limit, the energy contained in the shock is (following [De Colle et al. 2012](#)):

$$E_{nr} = \frac{(5-k)^2}{4} \alpha_k \frac{(3-k)}{4\pi} m_k c^2 \Gamma_s^2 \beta_s^2 \quad (\text{A22})$$

where α_k is a constant that depends on k . For $k = 0$ and $\gamma_{ad} = 4/3$, $\alpha_k = 1.25$ ([Taylor 1950](#); [Petruck 2000](#)). We can rearrange these equations by first defining some new constants as

$$x_0 = \frac{8\pi}{17-4k}, \quad y_0 = \frac{(5-k)^2}{4} \alpha_k \quad (\text{A23})$$

and then define a new function f_0 as

$$f_0 = \frac{E}{m c^2} \frac{4\pi}{3-k} \quad (\text{A24})$$

We then have in the ultrarelativistic limit the Lorentz factor of the shock found from

$$\Gamma_s^2 \beta_s^2 = \frac{f_0}{x_0} \quad (\text{A25})$$

and in the non-relativistic limit this becomes

$$\Gamma_s^2 \beta_s^2 = \frac{f_0}{y_0} \quad (\text{A26})$$

To account for the initial mass loading of the ejecta, we modify the values of E and m used in eqn. A24 as follows:

$$m = m_k + \frac{m_0}{\sqrt{\Gamma_0}} \quad (\text{A27})$$

$$E = E_0 \left[1 + \left(\frac{m_0}{m} \right)^A \Gamma_0^{(1+\frac{A}{2})} \right] \quad (\text{A28})$$

where m_0 is the initial (isotropic equivalent) mass of the ejecta and A is a constant determined by comparison to numerical results. For $k = 0$ we use $A = 0.225$.

To interpolate between the ultra- and non-relativistic limits, we define a new function z_0 to interpolate between x_0 and y_0 as

$$z_0 = \frac{C_1 x_0 f_0^{C_2} + y_0 / f_0^{C_2}}{C_1 f_0^{C_2} + 1 / f_0^{C_2}} \quad (\text{A29})$$

Based on comparison to numerical results, for $k = 0$ we use values of $C_1 = 1.6$ and $C_2 = 0.25$. We can then obtain the Lorentz factor of the forward shock in the blastwave phase from

$$\Gamma_{s,b}^2 \beta_{s,b}^2 = \frac{f_0}{z_0} \quad (\text{A30})$$

A4 Interpolation Between Phases

We now have Lorentz factor of the shock $\Gamma_{s,p}$, $\Gamma_{s,w}$, and $\Gamma_{s,b}$ for the piston, wind, and blastwave phases, respectively. To move between phases, it is convenient to work in term of $G = \Gamma_s^2 \beta_s^2$.

First, we interpolate between the piston and blastwave phases with the following procedure: We define $G_{0,b}$ as

$$G_{0,b} = G_b(R=0) = \Gamma_{s,b}^2 \beta_{s,b}^2 \quad \text{at } R=0 \quad (\text{A31})$$

The constant value for the piston phase, G_p , is always greater than $G_{0,b}$. We then define a threshold value to begin transitioning between these two phases at

$$G_t = G_{0,b} \left[0.8 \left(\frac{G_{0,b}}{G_p} \right) + 0.1333 \right] \quad (\text{A32})$$

We further define an interpolation variable V as

$$V = \frac{G_{0,b} - G_b}{G_{0,b} - G_t} \quad (\text{A33})$$

and an function F as

$$F = V^{(0.025+0.175(1-V)^4)} \quad (\text{A34})$$

We set the interpolated value G_i to

$$\begin{cases} G_i = G_p(1-F) + G_b F & G_b > G_t \\ G_i = G_b & G_b \leq G_t \end{cases} \quad (\text{A35})$$

The constants in the above equations are set for $k = 0$ by comparison to numerical simulations. This interpolation provides a smooth transition from the piston to blastwave phases.

The explosion will not always pass through the wind phase. The speed of the shock will only go to the wind phase value if G_w is less than the interpolated value G_i in eqn. A35 above. We therefore set the final value of $\Gamma_s^2 \beta_s^2$ as

$$\begin{cases} G = G_i & G_i > G_w \\ G = G_w & G_i \leq G_w \end{cases} \quad (\text{A36})$$

The Lorentz factor of the shock is then $\Gamma_s^2 = G + 1$. This gives the Lorentz factor and speed of the shock as a function of position R_s . The shock speed can then be integrated numerically to find the position of the shock as a function of time.

To find the Lorentz factor of the fluid just behind the shock, Γ_f , we numerically invert the expression for Γ_s^2 given in terms of Γ_f in eqn. A9. The density just behind the shock in the comoving frame is given by

$$\rho'_f = \rho_0 \frac{\gamma_{ad} \Gamma_f + 1}{\gamma_{ad} - 1} \Gamma_f \quad (\text{A37})$$

and the pressure is

$$P_f = \rho_0 (\Gamma_f - 1) (\gamma_{ad} \Gamma_f + 1) \quad (\text{A38})$$

A5 Interior Shock Structure

Interior to the shock front, we assume the structure of the Lorentz factor, density, and pressure are that of an impulsive blastwave. This will not be accurate during the piston and wind phases. We also do not include reverse shock emission which should be present during these phases.

For an impulsive explosion, the structure of the shock is different in the ultra-relativistic and non-relativistic limits. In the ultra-relativistic limit, the shock structure from [Blandford & McKee \(1976\)](#) is:

$$\begin{aligned}\Gamma_{rel} &= \Gamma_f \chi^{-1/2} \\ \rho'_{rel} &= \rho'_f \chi^{-(7-2k)/(4-k)} \\ P_{rel} &= P_f \chi^{-(17-4k)/(12-3k)}\end{aligned}$$

where

$$\chi = 1 + 4(m+1) \left(1 - \frac{R}{R_s}\right) \Gamma_f^2 \quad (\text{A39})$$

is a similarity variable and R_s is the radius of the shock. For a constant density external medium, $m = 3$.

In the non-relativistic limit, the structure behind the shock can be approximated in many forms (see [Petruk 2000](#)). We choose the Taylor approximation ([Taylor 1950](#)), with some relativistic corrections. We define a new similarity variable r defined as

$$r = \Gamma_f^2 \left(\frac{1}{\Gamma_f^2} + \frac{R}{R_s} - 1 \right) \quad (\text{A40})$$

At $R = R_s$, $r = 1$, and in the limit $\Gamma_f \rightarrow 1$, $r \rightarrow R/R_s$. The variable r is 0 at $R = \frac{\Gamma_f^2 - 1}{\Gamma_f^2} R_s$, and our approximation is not valid inside this limit. The Taylor approximation of the shock structure, with relativistic corrections, is:

$$\begin{aligned}\beta_{nr} &= \beta_f \frac{(\gamma_{ad} + 1)}{2} \left(\frac{r}{\gamma_{ad}} + \frac{(\gamma_{ad} - 1)}{(\gamma_{ad} + 1)} \frac{r^n}{\gamma_{ad}} \right) \\ \rho'_{nr} &= \rho'_f r^{3/(\gamma_{ad}-1)} \left(\frac{(\gamma_{ad} + 1)}{\gamma_{ad}} - \frac{r^{(n-1)}}{\gamma_{ad}} \right)^{-p} \left(r \frac{R_s}{R} \right)^2 \\ P_{nr} &= P_f \left(\frac{(\gamma_{ad} + 1)}{\gamma_{ad}} - \frac{r^{(n-1)}}{\gamma_{ad}} \right)^{-q} \left(r \frac{R_s}{R} \right)^2\end{aligned}$$

where the exponents (from [Petruk 2000](#)) are

$$\begin{aligned}n &= \frac{7\gamma_{ad} - 1 - k\gamma_{ad}(\gamma_{ad} + 1)}{\gamma_{ad}^2 - 1} \\ p &= \frac{2(\gamma_{ad} + 5 - k * (\gamma_{ad} + 1))}{7 - \gamma_{ad} - k(\gamma_{ad} + 1)} \\ q &= \frac{2\gamma_{ad}^2 + 7\gamma_{ad} - 3 - k\gamma_{ad}(\gamma_{ad} + 1)}{7 - \gamma_{ad} - k(\gamma_{ad} + 1)}\end{aligned}$$

To approximate the structure behind the shock, we interpolate between these two solutions, using β_f , the velocity just behind the shock. This gives the final velocity, density, and pressure as:

$$\begin{aligned}\beta &= \sqrt{\beta_{rel}^2 \beta_f^2 + \beta_{nr}^2 (1 - \beta_f^2)} \\ \rho' &= \rho'_{rel} \beta_f^2 + \rho'_{nr} (1 - \beta_f^2) \\ P &= P_{rel} \beta_f^2 + P_{nr} (1 - \beta_f^2)\end{aligned} \quad (\text{A41})$$

Our afterglow code solves these equations semi-analytically to find the equal-arrival-time surface of the shock for an observer at a given angle relative to the jet axis. The volume enclosed by this surface is then divided into s slices around the observer's line of sight. Each slice is then divided into y parallel lines of sight, and we calculate the hydrodynamic quantities at x equal-arrival-time points along each of those lines of sight. The typical number of slices, lines of sight and points are $s = 54$, $y = 30$, and $x = 100$, for 162,000 points total at a given arrival time.

APPENDIX B: SYNCHROTRON RADIATION

Synchrotron emission is calculated at a specified frequency along each line of sight, taking into account synchrotron self-absorption and synchrotron cooling. This returns a 2D image of surface brightness, which can then be integrated to give a total flux. At our typical resolution, the integrated flux is within 3 – 4% of the converged value at $\sim \infty$ resolution.

The local synchrotron emission and absorption coefficients are determined following [Rybicki & Lightman \(1979\)](#), assuming a fraction of the total energy in electrons ϵ_e , a fraction of the total energy in the magnetic field ϵ_B , and an electron powerlaw index of p . This is the

standard approach to synchrotron radiation, but a couple of points bear clarification: how the electron energy spectrum is determined and how synchrotron cooling is handled.

B1 Electron Energy Spectrum

Synchrotron radiation is modeled as being produced from relativistic electrons accelerated at the shock, such that they have a powerlaw distribution in Lorentz factor between some minimum Lorentz factor $\gamma_{e,min}$ and infinity. The number density of electrons as a function of Lorentz factor is

$$\begin{cases} N_e(\gamma_e)d\gamma_e = C_e \gamma_e^{-p} & \gamma_e \geq \gamma_{e,min} \\ N_e(\gamma_e)d\gamma_e = 0 & \gamma_e < \gamma_{e,min} \end{cases} \quad (\text{B1})$$

where C_e is a normalization constant. Taking the local values of the thermal energy density, E_{th} , and the electron number density n_e , C_e is calculated such that the total kinetic energy in electrons is $E_{k,e} = \epsilon_e E_{th}$ and the total number of electrons is n_e . In principle, not all the electrons need be accelerated, so the total number of accelerated electrons could be $f_e n_e$, where f_e is the fraction accelerated, but we use $f_e = 1$ by default. These constraints give a value of $\gamma_{e,min}$ of

$$\gamma_{e,min} = \frac{p-2}{p-1} \left(\frac{\epsilon_e E_{th}}{n_e m_e c^2} + 1 \right) \quad (\text{B2})$$

where the factor of 1 accounts for the rest-mass energy of the electrons. This gives a normalization of

$$C_e = (p-1)n_e \gamma_{e,min}^{(p-1)} \quad (\text{B3})$$

Note, however, that the value of $\gamma_{e,min}$ in eqn. B2 can be less than 1 if the thermal energy in electrons is small compared to the rest-mass energy of the electrons. This is an unphysical solution, but will eventually occur behind a relativistic shock because the material becomes cold. There are a few different ways to handle this situation:

- (i) Ignore the problem and allow $\gamma_{e,min}$ to be less than 1. This is unphysical, and it will shift the peak of the local synchrotron spectrum, ν_m , to lower energy.
- (ii) Make the electron energy distribution a powerlaw in the kinetic energy of the electrons, $\gamma_e - 1$, rather than the total energy. This would guarantee $\gamma_{e,min}$ is always greater than 1, but the electron distribution can no longer be easily integrated. At low temperatures, this also causes electrons to pile up about $\gamma_e \sim 1$. This would produce cyclotron radiation, not synchrotron.
- (iii) Calculate the electron distribution as above, but then truncate the distribution at $\gamma_e = 1$. This effectively reduces both the total energy in relativistic electrons (ϵ_e) and the fraction of electrons accelerated (f_e).
- (iv) Set $\gamma_{e,min} = 1$ and then calculate a new value of C_e such that the total kinetic energy in the electrons is correct. This effectively keeps ϵ_e constant, but reduces the fraction of electrons accelerated, f_e .

We choose the last option. This seems reasonable as it maintains $\gamma_{e,min} \geq 1$, and keeps the fraction of energy in electrons, ϵ_e , constant. It does, however, mean that the fraction of electrons accelerated will be less than 1 in some locations. Under these circumstances, where eqn. B2 would give a value less than 1, the new normalization constant is:

$$C_{e,1} = (p-1)(p-2) \frac{\epsilon_e E_{th}}{m_e c^2} \quad (\text{B4})$$

Setting this equal to eqn. B3, and replacing n_e by $f_e n_e$, the value of f_e is

$$f_e = \frac{C_{e,1}}{(p-1)n_e} = (p-2) \frac{\epsilon_e E_{th}}{n_e m_e c^2} \quad (\text{B5})$$

B2 Synchrotron Cooling

Synchrotron cooling occurs because high-energy photons are produced by high-energy electrons. Electrons are only accelerated at the shock front, but high-energy electrons radiate away a larger fraction of their energy per time than lower energy electrons. Eventually those high-energy electrons have cooled to lower energies, and the corresponding high-energy photons will not longer be produced.

The simplest way of modeling synchrotron cooling is to treat a shock as a monolithic slab of constant density and pressure gas, with a thickness corresponding to the amount of time the shock has existed. The oldest electrons will be at the back of the shock, and there will be a cooling break frequency, ν_c , corresponding to the frequency of the photons emitted by the highest energy electrons still present at the back of the shock. In front of this, closer to the shock, higher energy electrons will still be present, so photons with frequencies above ν_c will still be produced, but at a lower rate. In the slow cooling regime, with $\nu_m < \nu_c$, this corresponds to a decrease in the spectral slope of 1/2, from $F_\nu \propto \nu^{-(p-1)/2}$ to $F_\nu \propto \nu^{-p/2}$.

However, this slab model is not appropriate for a relativistic fireball. The pressure and density decrease behind the shock, altering the radiative properties and cooling time of the electrons. Instead, we need to find the cooling frequency at each point inside the shock, based on the integrated radiation it has emitted since it was shocked. The result is very gradual cooling break and more emission at high frequencies compared to using a single cooling frequency based on the maximum age of the shock.

From Granot & Sari (2002), the maximum Lorentz factor of the electron distribution at a coordinate χ inside the shock will be

$$\gamma_{e,max}(\chi) = \frac{2(19-2k)\pi m_e c \Gamma_f}{\sigma_t B_f^2 t} \frac{\chi^{(25-2k)/6(4-k)}}{\chi^{19-2k)/3(4-k)} - 1} \quad (\text{B6})$$

where B_f is the magnetic field at the shock front and t is the time when the material was shocked. We approximate t as

$$t = \frac{R_s}{c \left(1 - \frac{1}{2(4-k)\Gamma_s^2}\right)} \chi^{-\left(\frac{1}{4-k}\right)} \quad (\text{B7})$$

This gives a local cooling frequency of

$$\nu_c = \frac{3}{2} \frac{q B \gamma_{e,max}^2}{m_e c} \quad (\text{B8})$$

where q is the proton charge and B is the local magnetic field.

Along each line of sight, we calculate $\nu_c[i]$ at each point i . At the first point, just inside the shock, we set the emissivity to a cooling spectrum, $F_\nu[0] \propto \nu^{-p/2}$, above ν_c . For subsequent points, the emissivity is set to a cooling spectrum between $\nu_c[i]$ and $\nu_c[i-1]$, and to zero above $\nu_c[i-1]$, the cooling frequency of the point in front. This gives a reasonable approximation for synchrotron cooling, accounting for the changing conditions of the fluid behind the shock, but it is not exact.

In Fig. B1, we compare our model to the analytic model in Granot & Sari (2002) for a spherical blastwave. All of the powerlaw segments (dotted lines) and spectral breaks (solid vertical lines) are consistent with our semi-analytic spectrum, except for the cooling spectrum and the cooling break ν_c (solid red line). We find that the normalization of the cooling spectrum (region H in Granot & Sari 2002) is 5–8 times higher than in their analytic model. The frequency of the cooling break is proportional to the normalization squared, giving $\nu_c \approx 25-64$ times higher. In Fig. B1 the solid purple line is the analytic $-p/2$ segment multiplied by 6.5, and the vertical dashed red line is the analytic ν_c multiplied by $6.5^2 = 42$. The cooling break is very gradual, covering about 3 orders of magnitude in frequency, but is consistent with the shape given in Granot & Sari (2002).

This paper has been typeset from a \LaTeX file prepared by the author.

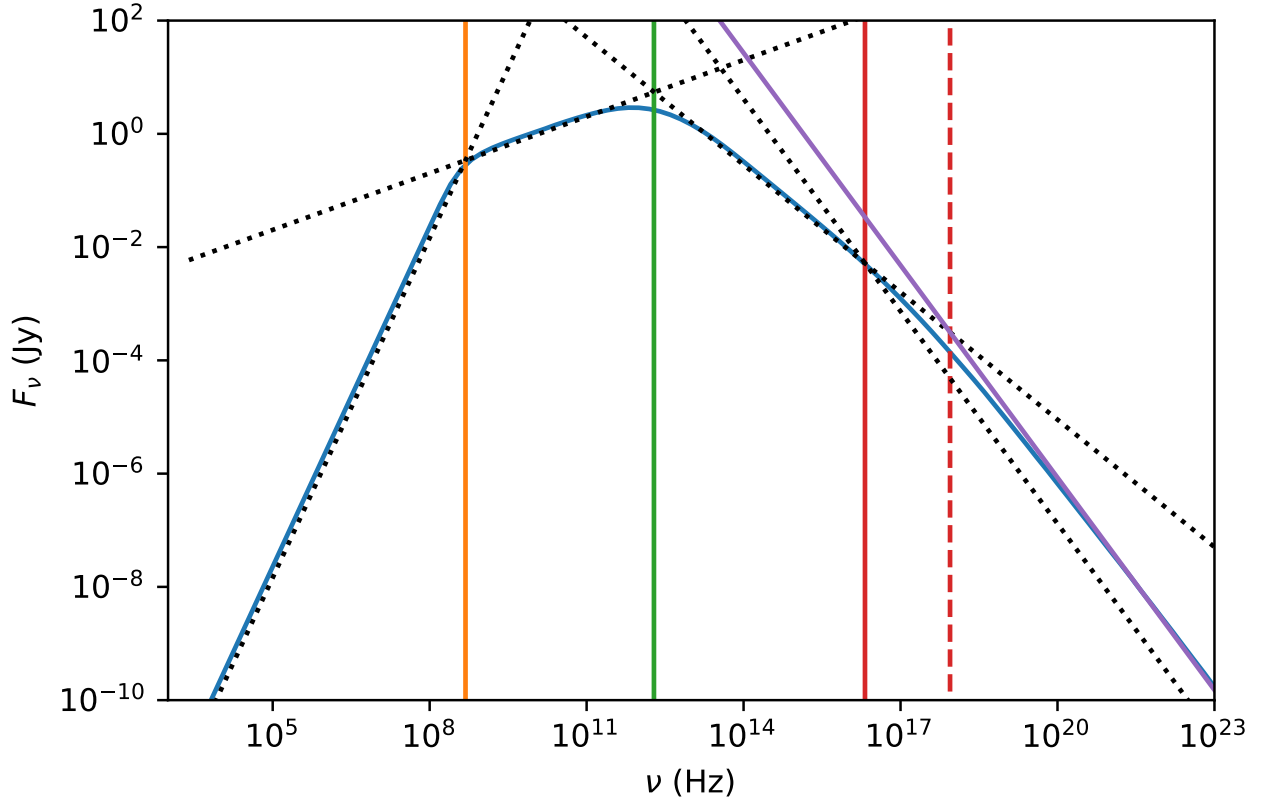


Figure B1. Semi-analytic TRAC spectrum (solid blue curve) for a spherical blast wave with $E_{iso} = 10^{52}$ ergs, $n_{ISM} = 10^{-2} \text{ cm}^{-3}$, $\epsilon_e = 0.1$, $\epsilon_B = 0.1$, and $p = 2.5$ at 10^3 s. Redshift is $z = 0.0098$ and luminosity distance is $d_L = 40.4$ Mpc, (appropriate for GW170817, Hjorth et al. 2016). Dotted black lines are powerlaw segments with analytic normalizations from Granot & Sari (2002), and solid vertical lines are their values for ν_{sa} (orange), ν_m (green), and ν_c (red). The solid purple line is the analytic $-p/2$ segment multiplied by 6.5, and the vertical dashed red line is the analytic ν_c multiplied by $6.5^2 = 42.25$.